Design Constraints of Small Single-Phase Permanent Magnet Brushless DC Drives for Fan Applications

Stephan Dunkl, Annette Muetze, *Senior Member, IEEE*, and Gerhard Schoener

***Abstract*—Permanent magnet brushless dc (BLDC) machines are widely used due to various advantages such as high efficiency and high torque density, and therefore compactness as well as long expected lifetime. All of these benefits are of major interest when designing a drive for a small fan application of a few watts. This paper presents the design investigations of a small single-phase BLDC motor for such an application. Notably, it discusses different constraints which arise during the design process and which may be of special relevance due to the particular given power level and application.**

***Index Terms*—Dynamic simulation, multidomain model, single-phase brushless dc (BLDC) fan.**

I. Introduction

BRUSHLESS dc (BLDC) motors have gained popularity due to their high efficiency, silent operation, compact form, reliability, and low maintenance [1], [2]. Permanent magnet (PM) BLDC motors use PMs for the rotor field excitation and an electronically commutated winding on the stator. Notably, with the use of rare earth magnets, these motors can have higher efficiency and be more compact when compared to induction motors and mechanically commutated dc motors. Single-phase PM BLDC motors, although less efficient compared to their three-phase counterparts, are cost-effective and easy to mass manufacture. They are used in applications which require output power ranging from a fraction of a watt to a few tens of watts [3], [4].

The target application was a small fan drive motor. To meet the specifications and because fan applications do not need high starting torques, an outer rotor single-phase BLDC appeared to be a good and cost-effective solution. Furthermore, it ensures simple motor construction and minimal electronic part count [5]–[7].

This paper discusses the design of a single-phase BLDC drive and presents different design constraints that arose. Furthermore, it discusses the relationship between different design parameters and the final motor performance. With this aim in mind, three different parameter studies will be presented. These parameter studies will vary the height and material of the magnets used, the number of turns of the winding, and the dimensions of the motor. While much of the analysis may appear to follow classical machine theory, aspects such as manufacturability and particular motor dimensions may require special treatment due to these machines' small sizes (Fig. 1). In the context of today's energy debate in which the energy conversion efficiencies of small energy converters have also become very important (not only their cost), we consider such discussion to be of renewed interest.

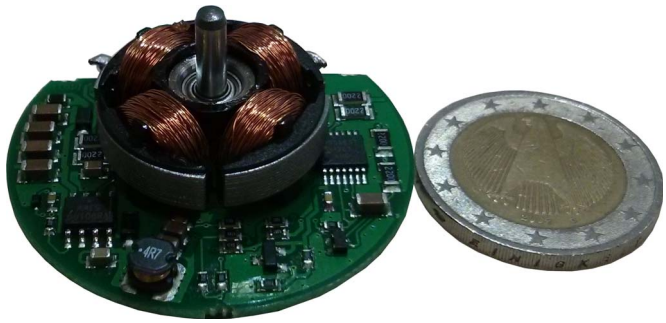

Fig. 1. Stator and drive circuit of a single-phase outer rotor BLDC fan motor.

This paper is divided into six sections. Sections II–V discuss the specifications and challenges of the motor design and how these were solved. In the main Section VI, different design constraints and relations between the design parameter and the motor performance are presented. The theoretical studies drawn from a multidomain model have been validated experimentally. Moreover, the experimental results of a prototype drive are provided.

Manuscript received September 3, 2014; revised January 26, 2015; accepted January 27, 2015. Date of publication February 24, 2015; date of current version July 15, 2015. Paper 2014-IDC-0599.R1, presented at the 2013 IEEE Energy Conversion Congress and Exposition, Denver, CO, USA, September 16–20, and approved for publication in the IEEE TRANSACTIONS ON INDUSTRY APPLICATIONS by the Industrial Drives Committee of the IEEE Industry Applications Society.

S. Dunkl and A. Muetze are with Graz University of Technology, 8010 Graz, Austria (e-mail: stephan.dunkl@tugraz.at; muetze@tugraz.at).

G. Schoener is with MSG Mechatronic Systems GmbH, 8551 Wies, Austria (e-mail: gerhard.schoener@mechatronic-systems.at).

Color versions of one or more of the figures in this paper are available online at http://ieeexplore.ieee.org.

Digital Object Identifier 10.1109/TIA.2015.2406856

II. Design Specification

The small fan drive to be designed should provide an output power of $P_{\mathrm{out}} = 1$ W at an operating speed of $n_r = 5000$ r/min at the motor shaft. Furthermore, the specifications of the small fan drive include some fairly restrictive operating conditions:

1) outer diameter of 30 mm;
2) guaranteed performance for a dc supply voltage of $U_{\mathrm{dc}} \in \{8\ \mathrm{V} \ldots 16\ \mathrm{V}\}$;
3) maximum current of $I_{\mathrm{max}} = 1$ A.

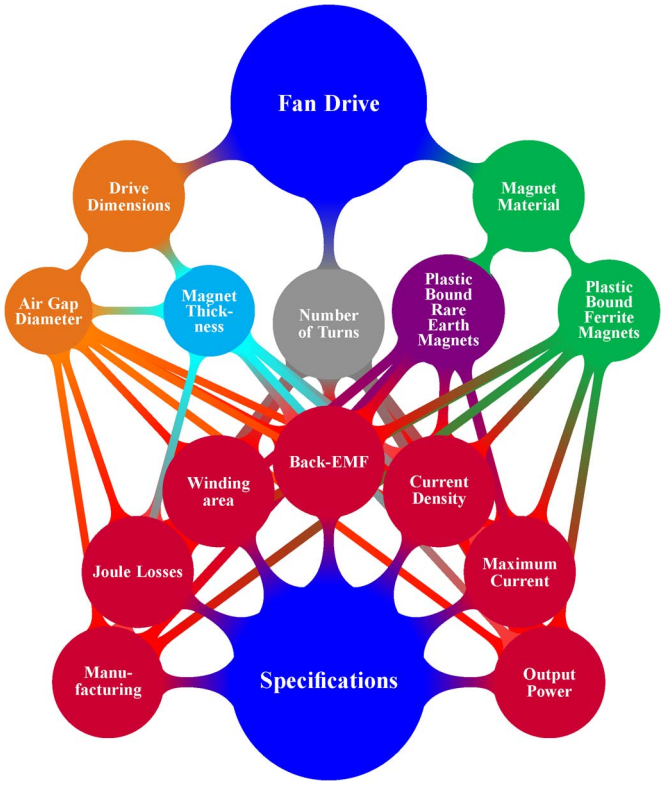

Fig. 2. Design constraints of the small fan drive.

Similar to most design tasks of small drives, the target application of the drive requires customized high-efficiency and low-cost design for small volume production.

III. Further Design Challenges

Due to the small size of the fan as well as the operating constraints and specifications, selection of the motor parameters such as outer motor diameter, material and thickness of the PMs, air gap length, number of turns, and wire diameter is subject to numerous tight constraints. Note that many of these are common for electrical machine design. However, because of the operating conditions, such as low supply voltage, high winding resistance, and high electrical time constant, some cannot be covered by analytic equations and show special sensitivity due to the small dimensions of the drive. Therefore, coupled finite element (FE) models (Section V) were built to illustrate new limits which arise for some motor parameters [8]–[11].

Fig. 2 gives an overview of the main parameter changes which will be made during the design process of a motor and the design constraints which will arise. This variation-mindmap is separated into two parts. The upper part shows the machine and design parameters that were to be determined in the application discussed, such as air gap diameter, number of turns, magnet thickness, and magnet material. The lower part lists the constraints which result from the parameters of the upper part of the mindmap. In general, the constraints are given by feasibility of manufacturing, efficiency, electrical constraints, and other given specifications of the application.

IV. Single-Phase BLDC Machines

Reviewing from [12], single-phase BLDC machines, in general, suffer from slower starting characteristics, less efficient utilization of machine iron and copper, and higher losses. Therefore, single-phase motors are limited to fractional power applications for which rapid response and high efficiency are not required. The primary advantage of single-phase devices is the simplified source requirements. For example, a single-phase BLDC motor requires only one-third of the number of transistors and position sensors needed by a three-phase motor.

In principle, single-phase BLDC machines have the same number of coils/slots as poles provided that they have a unifilar winding pattern. Thereby, the coils are connected in series and wound on the stator in a vice-versa manner. In order to generate torque over one electrical period of the motor, the current has to alternate its polarity, and consequently, the motor windings have to be fed by a full-bridge inverter. If the motor is built with a bifilar winding pattern, only two switches are needed for the alternating phase current of the machine.

For single-phase BLDC machines, two types of torque may occur with nonsalient PM motors [4]: 1) cogging torque, generated by the interaction of the PMs on the rotor and the stator teeth, and 2) excitation torque, generated by the interaction of the stator winding field and the field from the magnets. However, as these always have the same number of poles and slots, they have the drawback that excitation and cogging torque have coincident zero torque positions which make these motors unable to start from these dead point positions. To overcome this starting problem, these motors are designed with an asymmetric air gap, which shifts the zero points of the excitation torque from that of the cogging torque (e.g., [13]–[15]).

Often, external rotor designs are used for single-phase BLDC machines. These designs have a high moment of inertia and therefore are able to compensate the relatively high torque ripple of single-phase BLDC motors.

V. Modeling Approach

For the purpose of the investigations presented in this paper, two simulation models have been used. Section V-B shows a transient FE model simulating the maximum torque the motor is able to provide for a particular supply voltage at a duty cycle of 100% (PWM control).

In addition, several motor designs were studied with a multi-domain model, shown in Section V-C, which simulates the entire fan system. This multidomain model allows, for example, first predictions of energy conversion efficiency for the chosen operating point of the fan.

Both simulation models use an FE motor model that is reviewed in the following section.

A. Motor Model [17]

For the purpose of comprehensiveness, the motor model will be reviewed from [17]. Fig. 3 shows the final 3-D FE model of the electrical machine which is an outer rotor BLDC machine

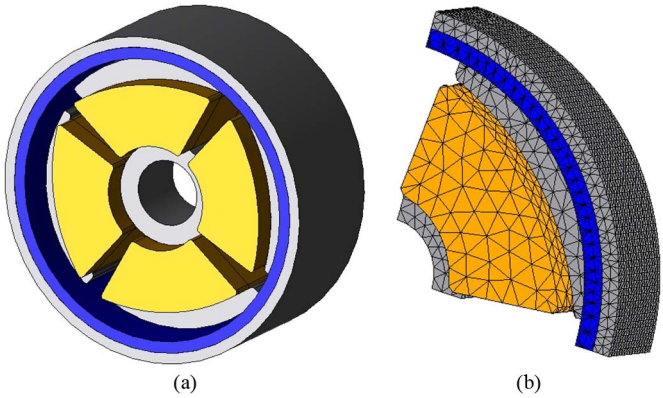

Fig. 3. FE model of the fan motor implemented in JMAG [16]. (a) Full model. (b) One-eighth model.

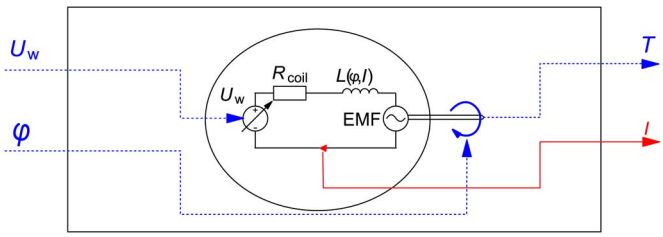

Fig. 4. JMAG connection block of the FE drive model.

using a four-pole four-slot combination. To reduce simulation time and exploit symmetry, only one-eighth of the total BLDC motor topology was implemented in the FE software [Fig. 3(b)].

The windings of a single-phase BLDC motor have a defined voltage potential at all times. This is exploited to couple the FE motor model to a circuit simulator. To link the JMAG motor model to the circuit simulator, the coils of the motor model are supplied with a controlled voltage source (U_w). This voltage source obtains its input values from a full bridge of the circuit simulation software (Appendix A-1). The second input parameter of the FE motor model is the displacement (φ) of the rotor from its initial value (Appendix A-2).

The output parameters of the model are the developed motor torque (T) and the winding current (I) for the actual calculated conditions of the drive. Fig. 4 shows the FE model with all its interfacing input and output parameters.

B. Maximum Torque Simulation

This simulation verifies whether a given design is able to supply the torque specified at rated speed and power. Fig. 5 shows a simple block diagram of the simulation.

The inverter circuit of the single-phase BLDC machine was also simulated in JMAG. The inverter stage uses a duty cycle of 100% for this simulation. Thus, the motor currents are only limited by the back EMF voltage and the rise time of the current, which is determined by the winding resistance and the coil inductance. As the current rises to its maximum, the simulated torque also rises to the maximum value which the motor is able to deliver at the simulated speed.

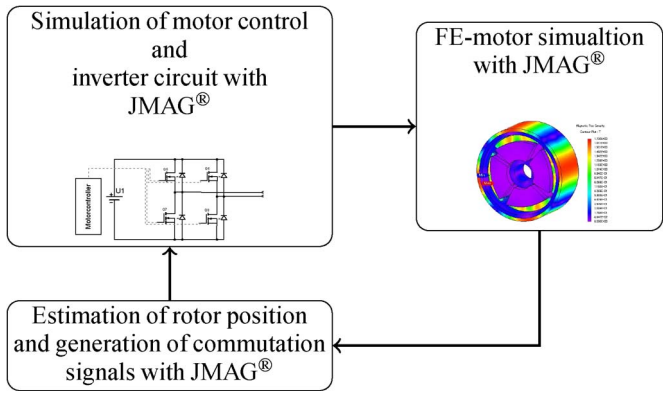

Fig. 5. Block diagram of the maximum torque simulation.

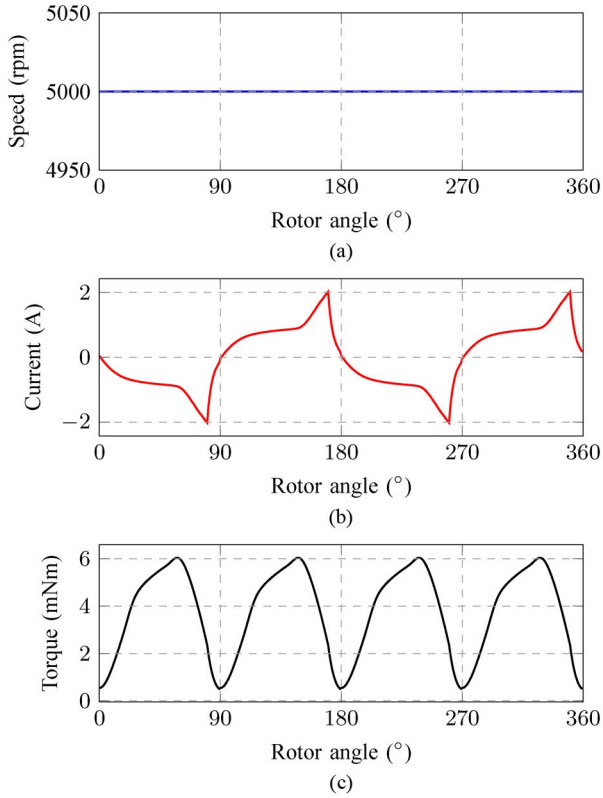

Fig. 6. Simulation results of the maximum torque simulation. (a) Simulated speed. (b) Simulated winding current. (c) Simulated maximum torque.

The commutation instances are generated by a look-up table which simulates the Hall sensor. This look-up table was calculated using preliminary simulations to ensure advanced commutation and that the winding current is in phase with the back EMF [18], [19].

Fig. 6 shows an example of the simulated torque and current waveforms for a given individual motor design.

C. Multidomain Fan Simulation

The multidomain model is used to predict the system's behavior and performance parameters such as energy conversion efficiency. The model has been described at length in [17]. For

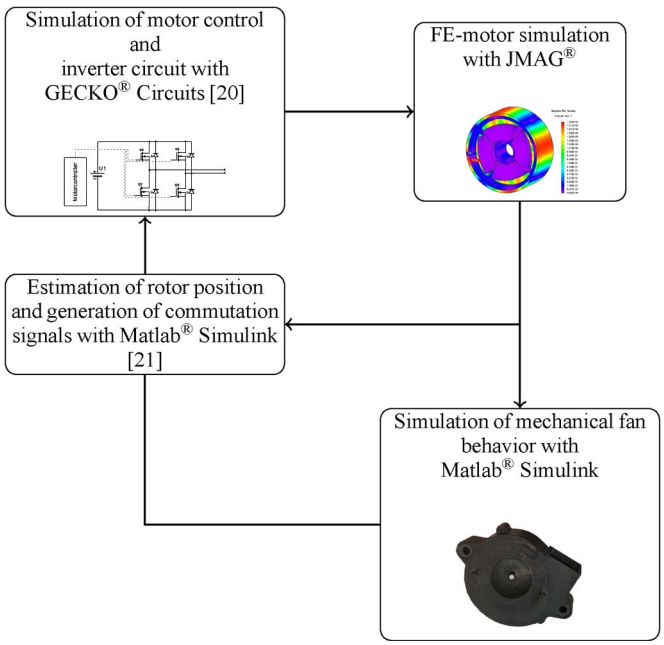

Fig. 7. Flowchart of the multidomain model [17].

the multidomain simulation, the fan system is split into several parts.

1) The first part simulates the electromagnetic behavior of the fan motor.
2) Since a BLDC motor was chosen as the drive topology, a simulation block responsible for the electric commutation of the motor phases was required. This commutation block comprises further logic to control the commutation instances.
3) To simulate the mechanical behavior of the fan system, the multidomain model had to be expanded with a block evaluating the motion equations based on the fan's moment of inertia and the speed-dependent load torque of the fan wheel.
4) Finally, as the fan's speed is controlled, the rotational velocity of the fan has to be determined. Therefore, a block was implemented, estimating the fan speed based on the signal of the Hall sensor.

Fig. 7 shows a flowchart of the multidomain model and gives an overview of its parts, as well as the software in which the individual parts were implemented. For detailed information on this model, we refer to [17]. For the sake of completeness of this paper, selected further information on the multidomain model is shown in Appendix A, and selected results from its experimental validation are provided in Appendix B.

VI. Results

A. Magnet Height

This first study focuses on the magnet height. In general, the magnet height defines the point of operation and therefore the magnetic flux that is driven through the motor. The lower boundary of the magnet height is limited by the manufacturing

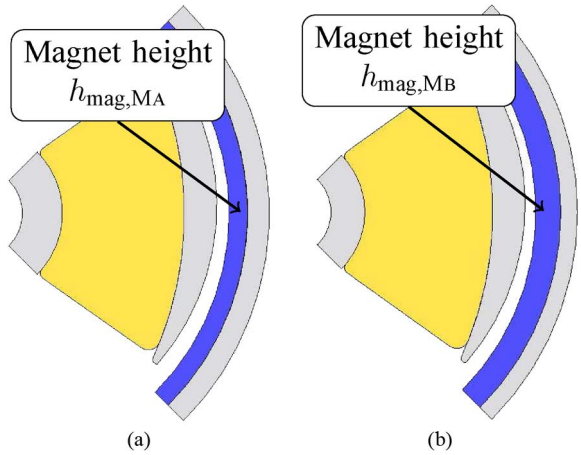

Fig. 8. Two identical designs, except for the different magnet thicknesses. (a) Motor MA with magnet height 1. (b) Motor MB with magnet height 2.

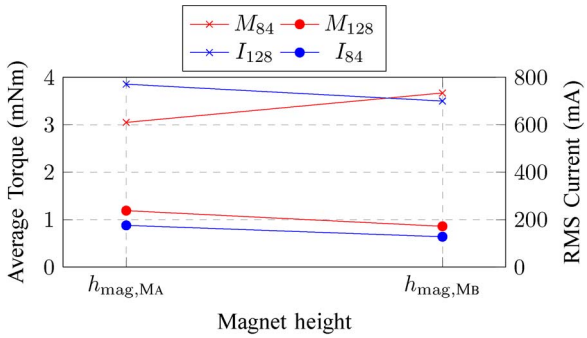

Fig. 9. Results for maximum torque simulation at $U_{\mathrm{dc}} = 8$ V and $n = 5000$ r/min.

capability. The upper limit is either set by cost or, for a chosen winding arrangement, by the resistance. The resistance shows special sensitivity in small power applications with regard to the inductance and induced EMF voltage of the motor coils (shown in the following discussion). The parameter variation study uses plastic bound ferrite magnets with different magnet thicknesses (motors MA and MB) for the motor models (Fig. 8).

The ratio of the magnet thicknesses of the two models is $h_{\mathrm{mag,MA}}/h_{\mathrm{mag,MB}} = 53\%$; the outer diameter of MB increases approximately by 9%. The stator dimension, as well as the rotor yoke thickness, is kept constant. The two motors are studied for two different numbers of turns but with identical copper cross-sectional areas. Fig. 9 shows the transient simulation results for the maximum average produced torque, rms current, and rms back EMF voltage for the four cases.

Due to the higher air gap flux density of MB, the back EMF voltage increases by 32% for an increase of magnet thickness of more than 50%. Furthermore, the current drawn by the motor decreases by $\approx$ 10%, and the maximum torque increases by $\approx$ 20% for 84 turns.

For the higher number of turns, this trend changes due to the coils' inductances and resistances, and since less of the source voltage remains to drive current through the coils (reduction by $\approx$ 27%), less torque will be produced (maximum torque decrease by $\approx$ 27%).

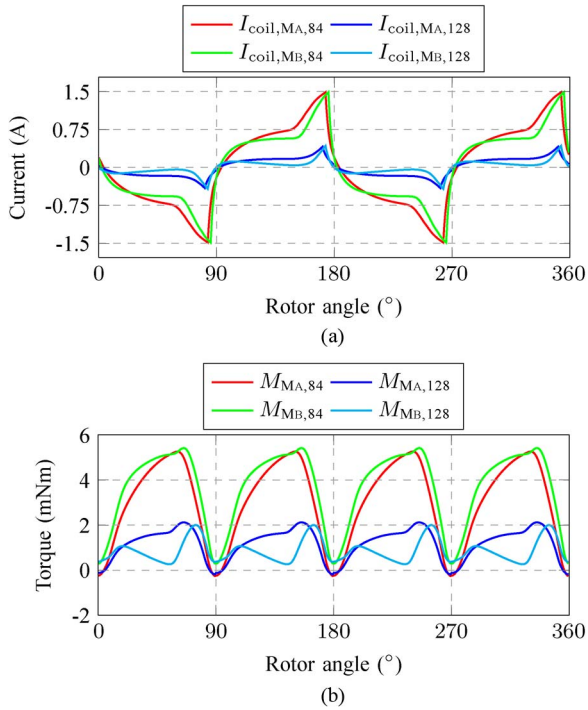

Fig. 10. Results of the maximum torque simulation of MA and MB. (a) Maximum winding current of MA and MB. (b) Maximum torque of MA and MB.

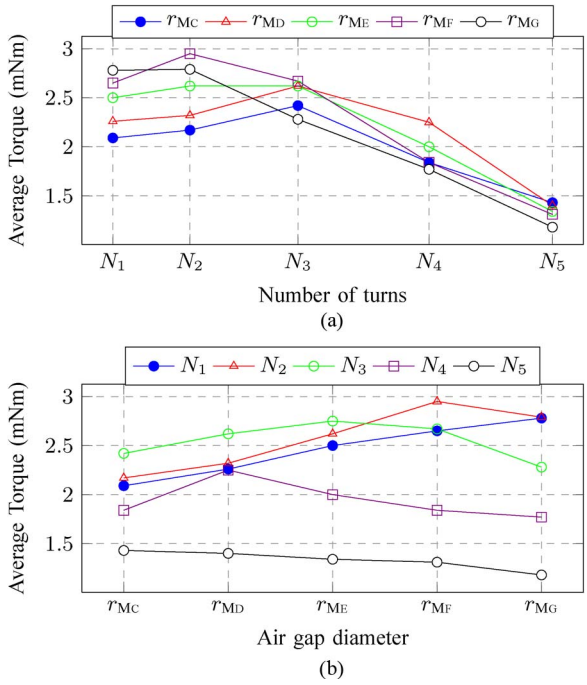

Fig. 11. Controlled torque simulation results for motors MC, MD, ME, and MF. (a) Motor torque for different numbers of turns. (b) Motor torque for different air gap diameters.

Fig. 10 shows the maximum current, as well as the maximum torque waveforms for the given supply voltage of $U_{\mathrm{dc,min}} = 8$ V at a duty cycle of 100% (maximum control output). Note that short current peaks are eliminated by the control without appreciable changes on the evolved torque. It can be noticed that the given value of $U_{\mathrm{dc,min}}$ presents a tough design challenge. Furthermore, the current drawn by the entire fan system will always remain below the simulated maximum current limit from Fig. 10(a).

B. Air Gap Radius

For the sake of comparison, the study analyzed five motors (motors MC–MG), with the same magnet material but with five different air gap radii (ratio $r_{\mathrm{MC}} : r_{\mathrm{MD}} : r_{\mathrm{ME}} : r_{\mathrm{MF}} : r_{\mathrm{MG}} = 0.8 : 0.9 : 1 : 1.1 : 1.2$). For these five different motor designs, the magnet, rotor, and stator yoke thickness are kept constant. Therefore, the air gap radius r_{MG} of motor MG sets an upper limit because further increasing the air gap radius would cause a wider magnet and higher flux. This would saturate the stator as well as the rotor yoke and result in a motor design with poor efficiency.

The different motors are analyzed with different number turns in the windings ($N_1 < N_2 < N_3 < N_4 < N_5$).

Taking a look at the torque equation

$$T \approx V\,B\,A \approx D\,B\,N\,I \tag{1}$$

where T describes the evolved torque, N is the number of turns, D is the air gap diameter, I is the current drawn by the motor, and B is the flux density of the PMs, we would expect the torque to rise with the increase of air gap diameters and number of turns.

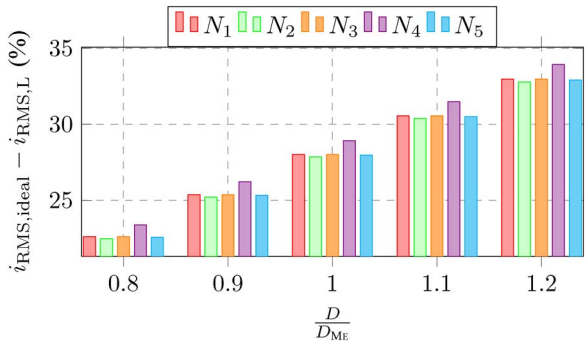

Fig. 12. Difference in drawn motor current due to the coil inductances.

For this comparison, the motors (having different air gap radii and number of turns) were analyzed with the maximum torque simulation. The latter was amended so that the current drawn by the machine was controlled to not exceed $I = 0.5$ A. In general, this simulation should keep the motor current from (1) constant, and a linear behavior between the air gap diameter or the number of turns and the torque could be expected.

Fig. 11(a) shows the torques of the motors with different numbers of turns. Differently than expected, the analyzed motors show a maximum in torque for a certain number of turns: For an increasing number of turns, the winding resistances increase too. At some point, the current drawn by the motors cannot reach the demanded value anymore, and the torque decreases. The higher number of turns also causes a higher flux linkage in the winding, which leads to less voltage remaining for driving the current through the winding. Fig. 12 shows the loss of motor current due to the increasing number of turns.

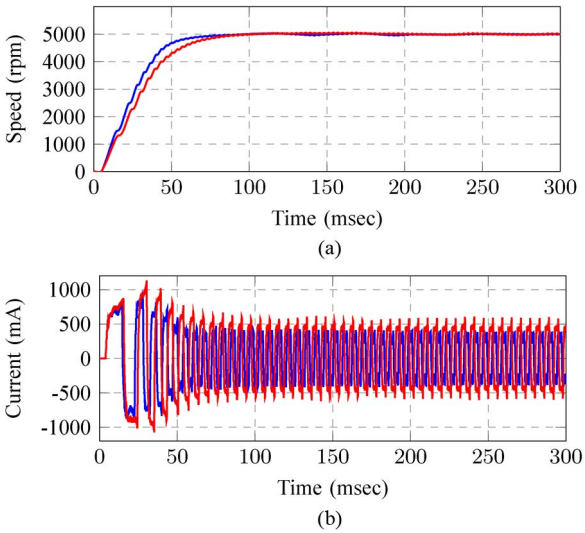

Fig. 13. Multidomain simulation results of drives —— MH and —— MI. (a) Simulated speed. (b) Simulated winding current.

TABLE I
MULTIDOMAIN SIMULATION RESULTS AT $U_{\mathrm{dc}} = 8$ V

Motor	Speed (avg) [rpm]	Current (rms) [mA]	Joule Losses [W]	Efficiency [%]
MH	5001	312	0.6	71
MI	4998	407	1.02	59

The same torque trend can also be seen in Fig. 11(b) for increasing air gap diameters. Again, increasing diameters cause higher flux linkages in the motor coils and higher motor inductances. Furthermore, for a motor with a fixed number of turns, the winding resistances stay constant. These two effects result in higher winding time constants and therefore in slower current rises which also have a negative effect on the evolved motor torque. Again, Fig. 12 shows the differences between the ideal rectangular current drawn by a resistive motor (without coil inductances) and the actual drawn current by the motor with different air gap radii.

C. Magnet Type

Again, the model from Fig. 3 is used to study two drives with the same dimensions. However, one motor (motor MH) uses rare earth magnets, whereas the other one (motor MI) uses ferrite magnets. Both models were simulated with the multidomain model of the entire fan system. A start-up procedure was simulated, and the results are shown in Fig. 13.

The ratio of the remanence between both magnets is $B_{r,h}/B_{r,i} \approx 132\%$. Table I shows the results of the multidomain model of the fan and drive system for steady state. Using ferrite magnets instead of rare earth magnets leads to a reduction of the remanence, but since the same torque is needed to drive the motor at rated speed, the electromotive force $(\theta = I\,N)$ has to be increased. As more current passes through the motor coils, more joule losses will be produced for the same winding, and the efficiency of the fan will decrease significantly (losses increase by $(I_{\mathrm{coil,MI}}/I_{\mathrm{coil,MH}})^2 \approx 1.3^2 = 1.69$). Also, due to the higher current drawn, the current density will increase by approximately 30%.

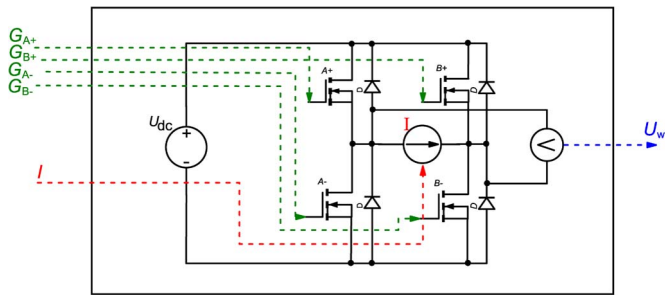

Fig. 14. Model of the inverter to drive the BLDC motor.

VII. CONCLUSION

In this paper, an outer rotor single-phase BLDC motor has been designed. This machine was designed by using steady-state and transient design and modeling techniques by simulating the entire fan system with a multidomain model. With these techniques, electrical and mechanical consequences of using different materials or dimensions were taken into account. Additionally, the design and modeling limitations were found. In particular, the combination of a certain supply voltage, winding resistances, and inductances and therefore the electrical time constants show a special sensitivity when designing small BLDC drives.

APPENDIX A
MULTIDOMAIN FAN MODEL

This appendix reviews further details of the multidomain model as they have been provided in [17].

1) Inverter Model: To supply the single-phase BLDC motor windings, an inverter model was built in the circuit simulation software Gecko Circuits. Fig. 14 shows the model, as well as its input and output parameters.

To consider effects such as freewheeling currents during commutation and PWM off cycles, the current flowing through the motor coils had to be linked to the inverter model. This coupling between the BLDC and the inverter model was accomplished with a current source which is controlled by the motor currents (Section V-A).

The output parameter of the inverter model is the voltage which is applied to the motor coils (U_w).

2) Mechanical Model: To simulate the mechanical behavior of the fan, as well as its load torque, a mechanical submodel was created. Acceleration and deceleration of the motor shaft are given by

$$\frac{d\omega}{dt} = \frac{1}{J}(T - k_b\omega - T_L) \quad \text{with}$$

$$\omega = \frac{d\varphi}{dt} \tag{2}$$

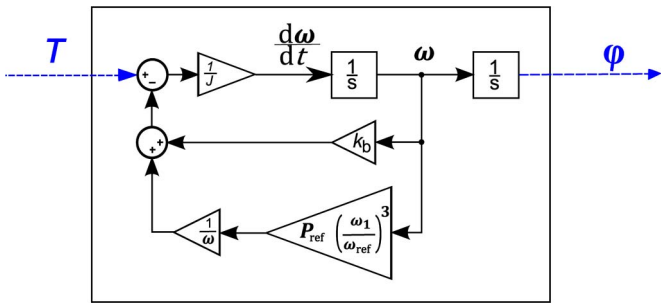

Fig. 15. Mechanical model of the fan drive.

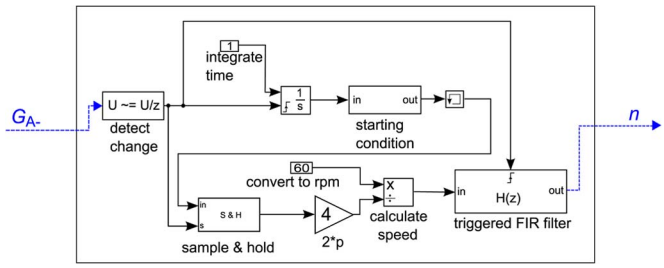

Fig. 16. Speed estimator of the fan drive.

where ω is the rotational velocity. J is the moment of inertia of the fan, and it was calculated from the materials and their specific weights. k_b is a factor accounting for friction, and T_L is the load torque of the fan wheel. The k_b factor was set up from empirical data, and to calculate the instantaneous load torque, the fan affinity laws from [22] were used.

Fig. 15 shows the mechanical submodel as well as its coupling links.

3) Commutation and Speed Estimation Model: The commutation of the BLDC drive is managed in relation to the rotor position through the inverter model shown in Fig. 14. As the fan drive uses a Hall sensor for detecting the rotor position and thus the commutation instances, a look-up table generating an appropriate Hall signal was implemented.

Since the fan's speed is controlled, the rotational velocity has to be measured. Therefore, the Hall signal is used to extract the speed of the fan drive. The speed can be determined as

$$n = \frac{1}{t_{\text{on}}\, 2\, p}\, 60 = \frac{1}{t_{\text{off}}\, 2\, p}\, 60 \quad [\text{r/min}] \tag{3}$$

where $2\,p$ is the number of poles of the motor. To ensure a stable speed estimation and filter out high frequency variations, the speed signals are averaged over four samples with a finite impulse response filter. Fig. 16 shows the speed estimator.

4) Speed Controller: The speed of the drive is controlled by a PI controller which generates the PWM signals for the inverter switches. Fig. 17 shows the flowchart of the speed control block.

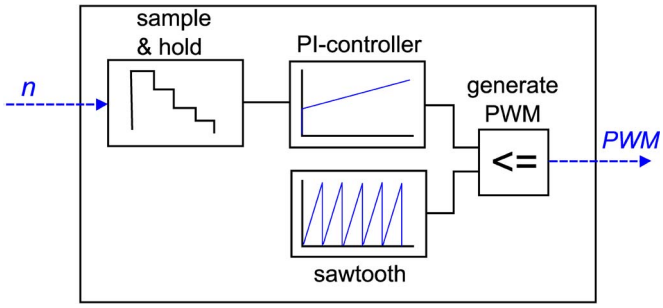

Fig. 17. Speed control block of the fan drive.

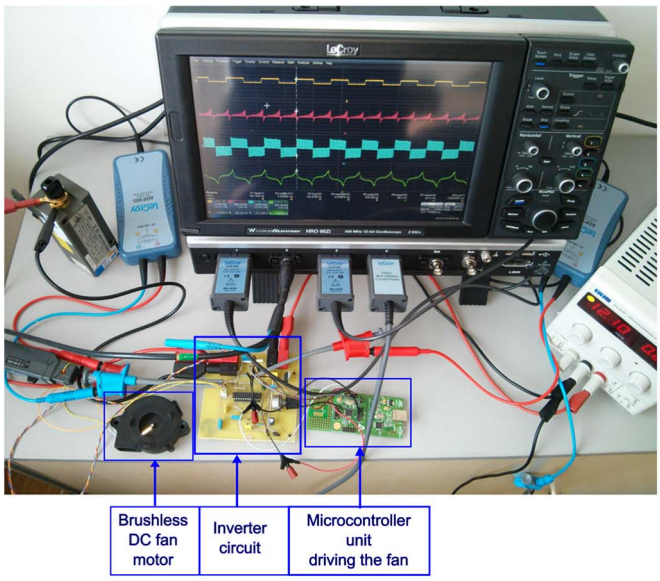

(a)

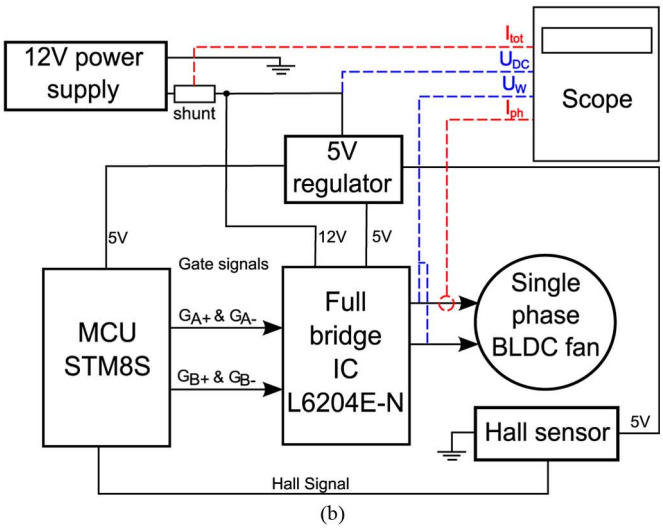

(b)

Fig. 18. Test setup to drive the BLDC fan motor. (a) Experimental test setup [17]. (b) Flowchart of the test system.

APPENDIX B
EXPERIMENTAL TEST SYSTEM

This appendix reviews the experimental test setup to validate the multidomain model presented in [17]. Fig. 18 shows the experimental test setup to drive the fan as well as the associated flowchart. It comprises the following.

1) The single-phase BLDC fan motor which is driven by the inverter IC.

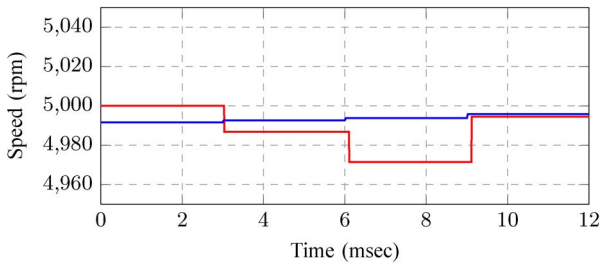

Fig. 19. Measured and simulated speeds (one rotation).

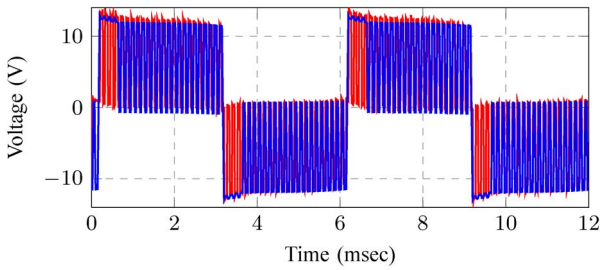

Fig. 20. Measured and simulated motor terminal voltages (one rotation).

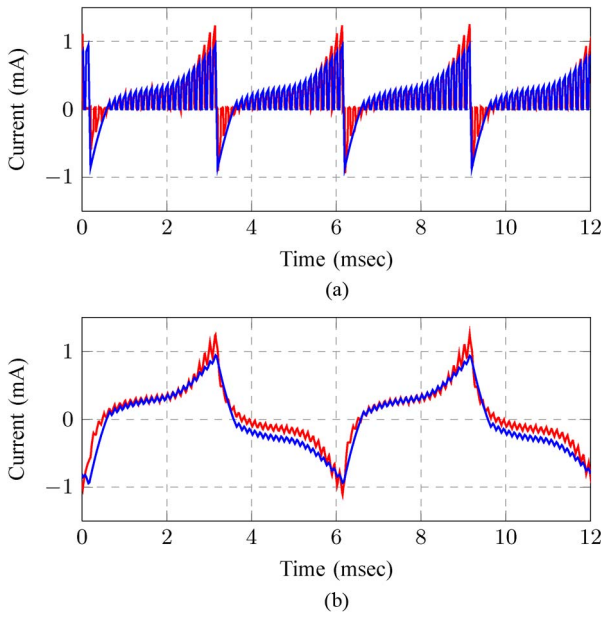

Fig. 21. Measured and simulated currents (one rotation). (a) Overall current of the fan motor. (b) Coil winding current of the fan motor.

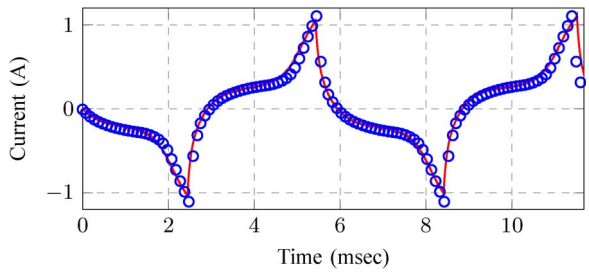

Fig. 22. Measured and simulated winding currents for maximum torque.

2) The Hall sensor generating a logic signal indicating the instantaneous rotor angle (pole facing the sensor).
3) The microcontroller unit (MCU) is responsible for calculating the speed of the drive. Furthermore, the control loop adjusting the PWM signals that are dependent on the drive speed and the generation of the input signals for the inverter IC according to the actual rotor position are implemented on the MCU.
4) The inverter IC converts the signals from the MCU to another voltage level and generates the signals to drive the BLDC.
5) The oscilloscope which measures the total and winding current and voltage.

Figs. 19–21 show the measured and simulated results for the estimated motor speed, motor terminal voltage, and drive currents for a steady-state condition for one design of the overall fan system. The multidomain model shows fairly good results compared to the measurement data. Note that the simulated winding currents and motor terminal voltages do not show the modulated PWM in their waveforms directly after commutation, whereas the measured currents and voltages do [17].

1) In the simulation, all MOSFETs are driven separately, whereas the MOSFETs of the inverter IC are driven by just two signals. Therefore, the simulated winding current cannot freewheel through the body diodes of the MOSFETs after commutation. The measured winding current behaves the same during PWM-ON, but for PWM-OFF, the motor winding is shortened by the two low-side MOSFETs of the full bridge.
2) In the simulation, the current can only flow through the power supply after commutation; therefore, the induced voltage at the motor terminal clamps must be higher than the voltage of the power supply.

In addition, the setup was also used to verify the maximum torque simulation. Fig. 22 shows a comparison of the simulated and measured maximum torque currents. For the maximum torque measurement, the MCU sets up the motor PWM with a 100% duty cycle. Then, an external stalling torque was applied to the motor until it reached a speed of $n_N = 5000$ r/min.

REFERENCES

[1] T.-H. Kim, H.-W. Lee, and M. Ehsani, "Advanced sensorless drive technique for multiphase BLDC motors," in *Proc. IEEE IECON*, 2004, vol. 1, pp. 926–931.
[2] A. Darba, F. De Belie, and J. Melkebeek, "Sensorless commutation and speed control of brushless dc-machine drives based on the back-EMF symmetric threshold-tracking," in *Proc. IEEE IEMDC*, May 2013, pp. 492–497.
[3] M. Fazil and K. Rajagopal, "Development of external rotor single-phase PM BLDC motor based drive for ceiling fan," in *Proc. Joint Int. Conf. PEDES Power India*, 2010, pp. 1–4.
[4] M. Fazil and K. R. Rajagopal, "Nonlinear dynamic modeling of a single-phase permanent-magnet brushless dc motor using 2-D static finite-element results," *IEEE Trans. Magn.*, vol. 47, no. 4, pp. 781–786, Apr. 2011.

[5] A. Lelkes and M. Bufe, "BLDC motor for fan application with automatically optimized commutation angle," in *Proc. 35th Annu. IEEE PESC*, Jun. 2004, vol. 3, pp. 2277–2281.
[6] L. Iepure, I. Boldea, and F. Blaabjerg, "Hybrid i-f starting and observer-based sensorless control of single-phase BLDC-PM motor drives," *IEEE Trans. Ind. Electron.*, vol. 59, no. 9, pp. 3436–3444, Sep. 2012.
[7] J. Mayer and O. Wasynczuk, "Analysis and modeling of a single-phase brushless dc motor drive system," *IEEE Power Eng. Rev.*, vol. 9, no. 9, p. 49, Sep. 1989.
[8] G. Kumbhar, S. Kulkarni, R. Escarela-Perez, and E. Campero-Littlewood, "Applications of coupled field formulations to electrical machinery," *COMPEL—Int. J. Comput. Math. Elect. Electron. Eng.*, vol. 26, no. 2, pp. 489–523, 2007.
[9] B. Asghari, V. Dinavahi, M. Rioual, J. Martinez, and R. Iravani, "Interfacing techniques for electromagnetic field and circuit simulation programs IEEE task force on interfacing techniques for simulation tools," *IEEE Trans. Power Del.*, vol. 24, no. 2, pp. 939–950, Apr. 2009.
[10] G. Jang, J. Chang, D. P. Hong, and K. Kim, "Finite-element analysis of an electromechanical field of a BLDC motor considering speed control and mechanical flexibility," *IEEE Trans. Magn.*, vol. 38, no. 2, pp. 945–948, Mar. 2002.
[11] S. Kanerva, "Simulation of electrical machines, circuits and control systems using finite element method and system simulator," Ph.D. dissertation, Dept. Elect. Commun. Eng., Helsinki Univ. Technol., Espoo, Finland, 2005.
[12] J. Mayer and O. Wasynczuk, "Analysis and modeling of a single-phase brushless dc motor drive system," *IEEE Trans. Energy Convers.*, vol. 4, no. 3, pp. 473–479, Sep. 1989.
[13] C. L. Chiu, Y. T. Chen, and W. S. Jhang, "Properties of cogging torque, starting torque, and electrical circuits for the single-phase brushless dc motor," *IEEE Trans. Magn.*, vol. 44, no. 10, pp. 2317–2323, Oct. 2008.
[14] S. Bentouati, Z. Zhu, and D. Howe, "Influence of design parameters on the starting torque of a single-phase PM brushless dc motor," *IEEE Trans. Magn.*, vol. 36, no. 5, pp. 3533–3536, Sep. 2000.
[15] M. Fazil and K. R. Rajagopal, "A novel air-gap profile of single-phase permanent-magnet brushless dc motor for starting torque improvement and cogging torque reduction," *IEEE Trans. Magn.*, vol. 46, no. 11, pp. 3928–3932, Nov. 2010.
[16] Simulation Technology for Electromechanical Design, JSOL Corporation, Accessed on 25-03-2013. [Online]. Available: https://www.jmag-international.com/
[17] S. Dunkl, A. Muetze, and G. Schoener, "Multi-domain modelling of a small single-phase brushless dc fan motor drive," in *Proc. IEEE 9th Int. Conf. IEMDC*, Chicago, IL, USA, May 12–15, 2013, pp. 1–6.
[18] C.-L. Chiu, Y.-T. Chen, Y.-H. Shen, and R.-H. Liang, "An accurate automatic phase advance adjustment of brushless dc motor," *IEEE Trans. Magn.*, vol. 45, no. 1, pp. 120–126, Jan. 2009.
[19] S.-M. Sue, K.-L. Wu, J.-S. Syu, and K.-C. Lee, "A phase advanced commutation scheme for IPM-BLDC motor drives," in *Proc. 4th IEEE ICIEA*, May 2009, pp. 2010–2013.
[20] Power Electronics Simulation Software, Gecko Research, Accessed on 28-08-2014. [Online]. Available: http://www.gecko-research.com
[21] Accelerating the Pace of Engineering and Science, MathWorks, Accessed on 28-08-2014. [Online]. Available: http://www.mathworks.de/index.html
[22] E. Stamper and R. Koral, *Handbook of Air Conditioning, Heating, and Ventilating*. South Norwalk, CT, USA: Industrial Press, 1979. [Online]. Available: http://books.google.at/books?id=G47biva6gtwC

Stephan Dunkl received the Dipl.-Ing. degree in electrical engineering from Graz University of Technology, Graz, Austria, in 2011, where he is currently working toward the Ph.D. degree.

He is a Research Assistant with Graz University of Technology. His research focus is on the design and analysis of fractional power brushless dc drives.

Annette Muetze (S'03–M'04–SM'09) received the Dipl.-Ing. degree in electrical engineering from Darmstadt University of Technology, Darmstadt, Germany, in 1999, the general engineering degree from the Ecole Centrale de Lyon, Ecully, France, in 1999, and the Dr.Tech. degree in electrical engineering from Darmstadt University of Technology in 2004.

She is a Full Professor with Graz University of Technology (TU Graz), Graz, Austria, where she heads the Electric Drives and Machines Institute. Prior to joining TU Graz, she was an Assistant Professor with the Department of Electrical and Computer Engineering, University of Wisconsin–Madison, Madison, WI, USA, and an Associate Professor with the School of Engineering, University of Warwick, Coventry, U.K.

Gerhard Schoener received the Ph.D. degree in experimental physics from the University of Graz, Graz, Austria, in 1983.

After a postdoctoral position at TACAN Corporation, Carlsbad, CA, USA, working in the field of fiber optic sensors, he worked on different sensor applications and passive electronic components in Austria. He is currently with Mechatronic Systems GmbH, Wies, Austria, working on mechatronic systems.